2023

Analog Holographic Wavefront Sensor for Defocus and Spherical Aberration Measurement Recorded in a Photopolymer

Emma Branigan
Technological University Dublin, emma.branigan@tudublin.ie

Suzanne Martin
Technological University Dublin, suzanne.martin@tudublin.ie

Matthew Sheehan
Technological University Dublin, matthew.sheehan@tudublin.ie

See next page for additional authors

Recommended Citation

Branigan, Emma; Martin, Suzanne; Sheehan, Matthew; and Murphy, Kevin, "Analog Holographic Wavefront Sensor for Defocus and Spherical Aberration Measurement Recorded in a Photopolymer" (2023). *Articles*. 100.
https://arrow.tudublin.ie/cieoart/100

Funder: Science Foundation Ireland (18/SIRG/5666).

Authors

Emma Branigan, Suzanne Martin, Matthew Sheehan, and Kevin Murphy

Research Article Vol. 31, No. 6 / 13 Mar 2023 / *Optics Express* 9466

Optics EXPRESS

Analog holographic wavefront sensor for defocus and spherical aberration measurement recorded in a photopolymer

EMMA BRANIGAN,[1,2,4] SUZANNE MARTIN,[1,2] MATTHEW SHEEHAN,[3] AND KEVIN MURPHY[1,2,*]

[1] *Centre for Industrial and Engineering Optics, School of Physics, Clinical and Optometric Sciences, Technological University Dublin (TU Dublin), D07 ADY7 Dublin, Ireland*
[2] *FOCAS Research Institute, Technological University Dublin (TU Dublin), 13 Camden Row, D08 CKP1 Dublin, Ireland*
[3] *School of Physics, Clinical and Optometric Sciences, Technological University Dublin (TU Dublin), D07 ADY7 Dublin, Ireland*
[4] *emma.branigan@tudublin.ie*
[*] *kevin.p.murphy@tudublin.ie*

Abstract: An analog holographic wavefront sensor (AHWFS), for measurement of low and high order (defocus and spherical aberration) aberration modes has been developed as volume phase holograms in a photopolymer recording medium. This is the first time that high order aberrations such as spherical aberration can be sensed using a volume hologram in a photosensitive medium. Both defocus and spherical aberration were recorded in a multi-mode version of this AHWFS. Refractive elements were used to generate a maximum and minimum phase delay of each aberration which were multiplexed as a set of volume phase holograms in an acrylamide based-photopolymer layer. The single-mode sensors showed a high degree of accuracy in determining various magnitudes of defocus and spherical aberration generated refractively. The multi-mode sensor also exhibited promising measurement characteristics and similar trends to the single-mode sensors were observed. The method of quantifying defocus was improved upon and a brief study into material shrinkage and sensor linearity is presented.

1. Introduction

Adaptive optics systems are used to correct aberrations of a wavefront that cause deviations from the ideal [1]. The result of these wavefront anomalies is usually a reduction in resolution, contrast and photon efficiency of optical systems. Real-time compensation for both low and high order aberrations (e.g. defocus and spherical aberration) can be applied through adaptive optics systems, typically comprised of corrective optics and a wavefront sensor (WFS). The role of the WFS is to detect the magnitude and type of the aberrations present in an incident wavefront. The pyramid [2] and curvature WFS [3] are just two examples of common WFSs. The Shack-Hartmann WFS (SHWFS) is the most widely used sensor across many applications in ophthalmology [4], optical communications [5] and astronomy [6]. While the operational principle of the SHWFS [7–9] is simple and robust, it is reliant on costly high-resolution imaging equipment and computationally expensive algorithms necessary for highly-accurate wavefront measurement. The SHWFS is essentially a multi-zonal tilt sensor, comprised of a multitude of discrete wavefront measurements. The slope data [10] obtained from these measurements can however be fitted to a modal set of polynomials [11,12]. The sensor is generally not well suited to the highly turbulent environments often faced in many long range or highly discontinuous sensing applications due to issues with scintillation, local obscuration and limited dynamic range.

#479357 https://doi.org/10.1364/OE.479357
Journal © 2023 Received 31 Oct 2022; revised 10 Jan 2023; accepted 12 Feb 2023; published 28 Feb 2023

The analog holographic wavefront sensor (AHWFS) is a highly efficient, cost-effective solution to these issues. Optical aberrations, described by a set of modes, are holographically recorded in a photosensitive medium. An orthogonal basis set such as the Zernike polynomials, can mathematically represent these modes and describe all aberrations for a continuous wavefront. A minimum and maximum phase delay associated with each mode is recorded as a pair of multiplexed holograms. When a wavefront containing arbitrary aberration modes is incident on the sensor, they will be optically decomposed into a set of paired diffracted beams for each mode. A normalized ratio of intensities at an array of photodetectors determines the magnitude of the aberration [13,14], while the angular position can be used to determine the aberration type, at speeds limited only by the detector readout. In theory, commercially available, inexpensive photodetectors will provide enough information to achieve bandwidth in the order of megahertz. The simple design of this inherently modal WFS omits the need for costly high-resolution imaging equipment, greatly reduces the computational overhead required for wavefront measurement and avoids any sensitivity to scintillation/obscuration.

Implementations of AHWFSs have been achieved using digital holographic recording techniques, where computer generated holograms of the aberration modes were produced using a Spatial Light Modulator (SLM) and holographically recorded, in dichromated gelatin (DCG) [15] and silver halide [16,17] and through etching a computer generated hologram into a silica substrate [18]. High levels of toxicity and an onerous development process are just some of the major material challenges of working with DCG. Distortion of holograms recorded in both DCG and silver halide can occur as a result of the chemical processing required to ‘fix’ the interference pattern recorded within the material. The need for a post-processing step can be avoided entirely by making use of a material that is self-developing. This is a favourable quality of an acrylamide-based photopolymer [19] and other self developing photopolymers [20–23] for mass production. High reproducibility, from one volume hologram to the next, can be achieved in the photopolymer. Good dynamic range of the material will facilitate multiplexing of several modes into one holographic optical element (HOE), allowing many aberrations to be detectable simultaneously.

In previous work the viability of a photopolymer based AHWFS for quantification of defocus [24] has been shown. Here, an improved holographic reconstruction technique to accurately measure three test magnitudes of defocus is presented. The recording and classification of a high order aberration, spherical aberration (SA), was carried out using refractive optical components for the first time, demonstrating the potential of this AHWFS as a multi-mode sensor for low and high order aberrations. Finally, both defocus and spherical aberration were multiplexed into a single HOE allowing for the simultaneous detection of both aberrations. The preparation of the photopolymer layers used to record the HOEs, optical setups and methodology used for the recording and reconstruction of the holograms are described in the Materials and Methods section. The Results and Conclusions sections outline the key achievements and results from both single-mode and multi-mode AHWFSs.

2. Numerical modelling

2.1. *Third order approximation of spherical aberration*

Wavefront aberrations can be considered in terms of geometrical ray intercept errors at the image plane [25], or as optical path length differences. Here, the former technique was used to quantify the magnitude of spherical aberration introduced by a series of refractive elements [26]. This treatment of the geometrical aberrations was first published by Ludwig von Seidel and includes all of the third order terms in a centered system of spherical surfaces [27]. Longitudinal spherical aberration (LSA) can be defined as the longitudinal difference between the paraxial and the marginal foci. LSA can be related to the Seidel aberration coefficient by

$$A = \frac{\Delta z}{3R^2 y^2} \tag{1}$$

where A is the Seidel aberration coefficient, Δz is the magnitude of LSA, R is the reference sphere radius and y is the ray height.

2.2. Refractively generated spherical aberration

Oftentimes fast, singlet lenses are avoided in imaging optics due to the fact that they are prone to aberrations. In this instance, it was both convenient and of benefit to make use of the appreciable spherical aberration inherent to these lenses for the fabrication of the sensor. Positive spherical aberration could be introduced by arranging two different biconvex lenses into a 4f imaging system. In a perfectly symmetric 4f system, where both lenses are identical, it is expected that the sum of SA generated is 0. However, by using lenses with different optical powers the contribution of both the anterior and posterior surfaces of the lenses to the total aberration magnitude can be considerable. Combinations of various lenses arranged in a similar manner allowed for the generation of a number of test aberrations within the bounds of a given sensing range. Zemax optical design software was used to model the biconvex singlets in order to determine the magnitude of positive SA introduced. The resultant Seidel spherical aberration coefficient, A, was used to calculate the magnitude of a Δz shift introduced by the refractive elements over a given aperture (Eq. (1)). Knowing the central spatial frequency of the recorded holographic interference pattern, the diffraction grating equation

$$2d\sin\theta = m\lambda_i \tag{2}$$

where d = grating spacing, θ = the Bragg angle, m = diffraction order, λ_i = probe wavelength, in the medium, was used to calculate the expected Bragg reconstruction condition, θ, in the medium. Snell's law was employed at the boundaries to translate the required angles in the medium, to angles in air. This was carried out for HOEs with no spherical aberration versus those with some magnitude of positive SA present. The result was a difference in angle of incidence at a specific location on the WFS hologram for the unaberrated and aberrated case, which was equivalent to the maximum angular detuning caused by the introduction of the refractive elements.

2.3. Hologram sensitivity

While the effect of a significant spherical aberration can be clearly observed in imaging systems [28,29], this minor change in the wavefront shape can be difficult to detect. A maximum deviation from an ideal reference wavefront is seen at the extreme edges of a circular beam and can be increased with increasing aperture. As a collimated beam was selected as the minimum sensing bound of the AHWFS for SA detection there was little change in the shape of the wavefront in the central portion of the recording beam. A theoretical model was developed to predict the maximum Bragg angle detuning that could be introduced by refractively generated SA.

The model, based on Kogelnik's Coupled Wave Theory (KCWT) [30], was used to investigate the angular selectivity of the recording medium at various layer thicknesses and central spatial frequencies. KCWT can be applied to holographic gratings that satisfy the conditions necessary to be classified as 'thick' or volume phase holograms. In transmission mode, light is diffracted into a single order only. The diffraction behaviour is described by

$$\eta = \frac{\sin^2\sqrt{\nu^2 + \xi^2}}{1 + \frac{\xi^2}{\nu^2}} \tag{3}$$

where ν and ξ are given by

$$\nu = \frac{\pi t \Delta n}{\lambda_r \sqrt{\cos\theta_R \cos\theta_S}} \tag{4}$$

$$\xi = \frac{\Gamma d}{2\cos\theta_S} \tag{5}$$

and t = material layer thickness, Δn = refractive index modulation, λ_r= reconstruction wavelength, θ_R = angle of incidence in the material, θ_S = angle of diffraction in the material, Γ = mismatch constant for deviations from the Bragg condition. The hologram characteristics can be varied in order to tune the diffraction behaviour of the desired hologram. By examining the full-width at half-maximum of diffraction efficiency (DE) or Bragg curves (Fig. 1), modelled at 100% DE, it was possible to predict the maximum angular detuning that could be tolerated by the material. Therefore, the sensitivity of the device can be greatly enhanced by increasing both the layer thickness and carrier spatial frequency of the hologram (Fig. 2).

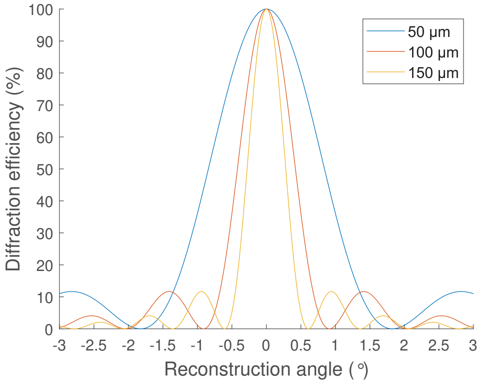

Fig. 1. Bragg curves, or theoretical dependence of hologram efficiency on reconstruction angle for a hologram with 100% on-Bragg efficiency with a spatial frequency of 816 lines/mm, at 3 material layer thicknesses of 50 μm (blue line), 100 μm (red line) and 150 μm (yellow line) and a probe wavelength of 532 nm. The x-axis represents the incident angle in air i.e. the angle at which the hologram is reconstructed.

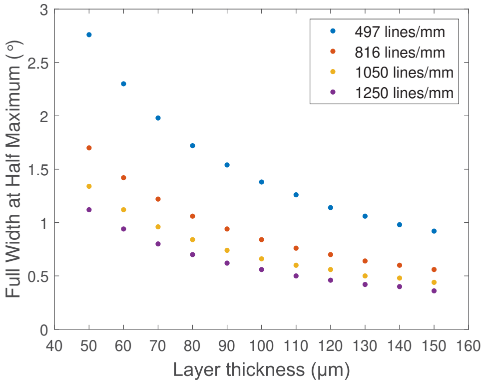

Fig. 2. The full-width at half-maximum of Bragg curves, modelled at 100% diffraction efficiency, for various layer thicknesses and carrier spatial frequencies of: 497 lines/mm (blue marker), 816 lines/mm (red marker), 1050 lines/mm (yellow marker) and 1250 lines/mm (purple marker).

3. Materials and methods

3.1. Material and sample preparation

The photopolymer solution was prepared using the following method. A 10 % w/w stock polyvinyl alcohol (PVA) solution was prepared in deionised water. A stock dye solution with a concentration of 1.1 mg/cm^3 of Erythrosine B was also prepared in water. Then, 2.0 ml of triethanolamine, 0.2 g of bisacrylamide and 0.8 g of acrylamide monomers [31] were added to 17.5 ml of the PVA solution. Finally, 4 ml of stock dye solution was added. The mixture was stirred continuously until all of the monomers had dissolved.

The appropriate volume of photopolymer solution was pipetted out onto a 75 x 25 mm glass slide and left to dry on a levelled plate. A wet volume of 657 µL, spread on the slide, gave a dry layer thickness of nominal 65.7±12.14 µm. The samples were left to dry for 24-36 hours and then covered to preserve and protect them from changes in humidity. High angular selectivity of the HOEs was not required for defocus detection due to the significant distortion of the wavefront. However, in order to achieve the sensitivity necessary to detect spherical aberration thicker layers were also prepared. A wet volume of 1500 µL, spread on the slide, gave a dry layer of 150 ± 12.20 µm and required 60-72 hours of drying time. Once dry, the layer was laminated with a 50 µm layer of Melinex polyethylene terephthalate (PET) film.

3.2. Holographic recording

For fabrication of the analog holographic wavefront sensor (AHWFS), recording of a transmission, volume Bragg HOE was carried out with a 532 nm wavelength Nd:YAG laser. The spatially filtered beam was collimated and directed towards the photopolymer holographic recording material using a beam splitting system (Fig. 3). The sample was fixed in place with the covered photopolymer layer facing the surface of the beamsplitter. The slide was arranged so that B_T was at normal incidence to the sample. A series of plane mirrors were used to direct the beam, B_R, towards the photopolymer sample, at angles associated with a number of spatial frequencies. The beams B_T and B_R were overlapped in the plane of the sample to produce an interference pattern that was recorded in the volume of the material.

To define the minimum/maximum sensing range for a single aberration mode within the AHWFS, two known wavefronts were holographically multiplexed into a single photopolymer layer. The full recording setup for recording both the defocus and spherical abberation modes is shown in Fig. 3. Two separate single-mode wavefront sensors were fabricated; one for defocus detection and a second for SA detection. A third, multi-mode, AHWFS was then developed for simultaneous detection of the two aberration modes by multiplexing a maximum and minimum associated with each mode into a single HOE.

A biconvex lens, L1 (f = 150 mm), was positioned along a rail a distance away from the sample, to generate a maximum (217 mm from the sample) and minimum (83 mm from the sample) phase delay/advance of the defocus mode (Fig. 3(a) & 3(b)). The result was the separate recording of a holographic converging lens ($L1_{\text{min}}$) and a holographic diverging lens ($L1_{\text{max}}$) in the photopolymer layer with focal lengths of 67 mm. This produced an equal and opposite magnitude, ±15.0 D, of defocus for the two holographic lenses over a diameter of 4 mm.

The minimum limit of the SA sensing range was introduced by holographically recording a collimated beam, 4 mm in diameter, corresponding to 0 µm of spherical aberration (Fig. 3(c)). For the maximum SA, a standard 4f imaging system consisting of a f = 50 mm biconvex lens (L2) and a f = 35 mm biconvex lens (L3) was then used to translate the beam onto the photopolymer sample (Fig. 3(d)). The spherical aberration inherent to this lens arrangement was used to produce the maximum limit of the sensing range. Zemax optical design software was employed to model the lens configuration at $\lambda = 532$ nm, with an input beam diameter of 5.71 mm. The magnitude of spherical aberration introduced was 0.67 λ peak-to-valley or +2.85 µm, given in

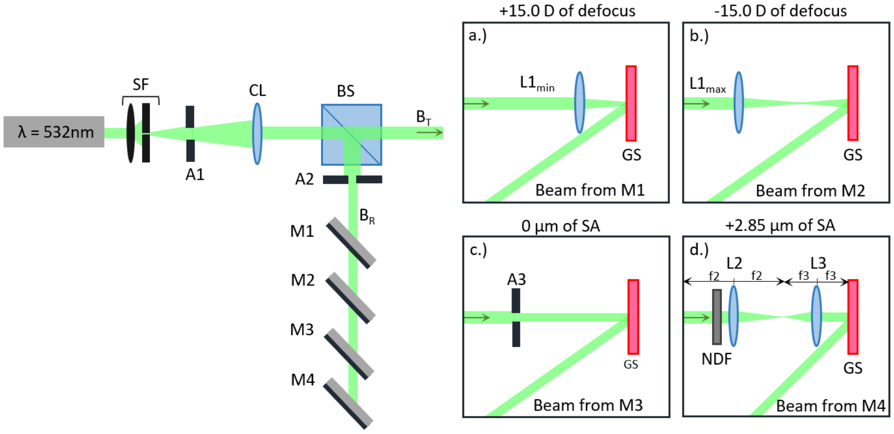

Fig. 3. Holographic recording setup for generating: (a) +15.0 D of defocus, (b) -15.0 D of defocus, (c) 0 µm and (d) +2.85 µm of spherical aberration using solely refractive elements. Optical components are: SF: spatial filter, A1: 10 mm aperture, CL: collimating lens, BS: beamsplitter, A2 & A3: 4 mm apertures, M1, M2, M3 & M4: planar mirrors, GS: Glass slide with photopolymer layer, NDF: 0.3 optical density neutral density filter, L1: f1 = 150 mm biconvex lens, L2: f2 = 50 mm biconvex lens, L3: f3 = 35 mm.

Seidel aberration coefficients. The relationship between the wavefront aberration and Seidel aberration coefficients for primary spherical aberration is given as

$$A = 8W_{040} \tag{6}$$

where W_{040} is the wavefront aberration coefficient.

Angular multiplexing techniques were used to separate the diffracted output of the holograms recorded in the HOE. A higher angular selectivity of the recorded hologram was achieved by increasing the angular separation between the two interfering beams. This allowed for greater sensitivity to small wavefront distortions caused by the introduction of SA. The spatial frequency along the horizontal axis of each HOE was calculated using the recording geometry and the diffraction grating equation (Eq. 2). Four plane mirrors, mounted on flip plates, were used to introduce four separate carrier spatial frequencies (CSF). Mirrors M1 and M2 were used in the recording of holograms 1 and 2 (H1 and H2) for defocus detection. H1 was recorded, with L1 in the minimum position, at a CSF of 497 lines/mm. M1 was then flipped down to allow the beam to propagate to M2, where it was directed towards the photopolymer sample. H2 was recorded with L1 in the maximum position, at a CSF of 816 lines/mm. Mirrors M3 and M4 were used for the recording of holograms 3 and 4 (H3 and H4) to detect spherical aberration. The beam was reflected off M3 and interfered with a collimated beam to record H3 at a CSF of 1050 lines/mm. M3 was then flipped down, and M4 directed the beam towards the sample to introduce a subsequent hologram (H4) with +2.85 µm of SA and a CSF of 1250 lines/mm. As all of the holographic holograms are volume Bragg holograms diffraction will only occur in the first order once each specific Bragg condition has been satisfied.

The exposure time of the layer to the laser was controlled by an electromechanical shutter. This was necessary to achieve each desired diffraction efficiency range. Initial work on an AHWFS for defocus detection involved investigating the sensitivity of sensors with different diffraction efficiencies [24]. Therefore, laser intensity equivalent to 0.28 mW/cm^2 was delivered to the sample, over a range of exposure times from 5 to 26 seconds. A short delay (~1 min) was introduced between the recordings as each mirror was flipped out from the optical path and the refractive elements were moved into position along the rail. A NDF with an optical density of 0.3 was used to equalize the intensity between beams B_T and B_R, following the addition of lenses for defocus and SA generation. For the single-mode sensors, a longer exposure time was needed to record H2 and H4 as some of the dynamic range of the photopolymer had been depleted during the first recordings (H1 and H3). An iterative process was used to determine the exposure duration necessary for the successful recording of four holograms into a single element, for fabrication of the multi-mode sensor. Equalization of the DE of each recording was necessary to ensure good measurement accuracy of each sensor. The samples were left under the overhead room lights to bleach slowly over a period of ~12 hours. This step was particularly important for samples with a very low DE, in order to fully polymerise any remaining monomer in the layer prior to the holographic reconstruction process.

3.3. Hologram reconstruction and unknown aberration detection

3.3.1. Measurement of diffraction efficiency

Theory predicts that for a perfectly efficient volume hologram, 100 % of incoming light is diffracted into the first order spot for which the Bragg condition is satisfied. However, in practice some small proportion of the beam is typically transmitted through into the zero order. Here the use of multiplexed volume phase holograms, recorded over a range of diffraction efficiency strengths, were used to quantify both defocus and spherical aberration. It was of particular interest to investigate the response of low diffraction efficiency holograms to gain information about the number of potential aberration modes that could be multiplexed into a single volume element. To measure the efficiency of the recorded HOEs, the samples were clamped in place in the same orientation used in recording i.e. with the photopolymer layer normal to B_T. To ensure the hologram was reconstructed correctly, careful alignment of the HOE to the incoming beam was necessary. B_R was blocked so that only the beam B_T was used in reconstruction. When the probe beam was phase matched to the beam used to record the hologram of interest, the intensity of the diffracted output associated with the angular position of that hologram was a maximum. Some portion of the beam was transmitted and a small fraction diffracted into the spots associated with other holograms.

A silicon PIN photodiode (Thorlabs FDS1010), connected to the analog input of an Arduino Due was used to measure the beam intensities in order to calculate the diffraction efficiency of each recording. The intensity of the transmitted beam (I_T), the spot for which the Bragg condition was satisfied (I_{Hn}) and the other diffracted spots (I_{Hm}) was measured. The efficiency of the hologram under probe, H_n, was calculated by Eq. (7)

$$DE_{Hn} = \frac{I_{Hn}}{I_T + \sum\limits_{m=1}^{m=N} I_{Hm}} \tag{7}$$

where N is the total number of holograms recorded in the HOE and m, n and $N \geq 1$ and $\in \mathbb{N}$.

3.3.2. Improved methodology for defocus quantification by the AHWFS

Quantification of various magnitudes of refractively generated defocus has previously been shown by an AHWFS [24]. The repeatability and accuracy of the hologram reconstruction method used previously has been improved upon. A number of biconvex lenses, mounted on a rail system, were positioned so that the diameter of the converging beam incident on the sample was 4 mm in diameter. This ensured that the size of the HOE was perfectly matched and not over/underfilled. The focal length of the given lens (L4) determined the magnitude of the aberration. Lenses with focal lengths of: 250 mm, 300 mm and 400 mm, were used to introduce +4.9 D, +7.1 D and +9.0 D of defocus respectively (Fig. 4(a)). Physical stops were set up along the rail to reliably replicate the magnitude of the test aberrations with the introduction and removal of each lens.

The magnitude of defocus was determined through a normalized ratio of intensities (NIR) between the H1 and H2 diffracted outputs. Depending on the magnitude and sign of the incident wavefront, more or less light was diverted into each spot. As the maximum and minimum sensing bounds of the device were equal and opposite, it was possible to calculate the magnitude of defocus (W_D) contained in an incident wavefront by

$$W_D = R_D \frac{I_{H1} - I_{H2}}{I_{H1} + I_{H2}} \tag{8}$$

where $R_D = 15.0$ D.

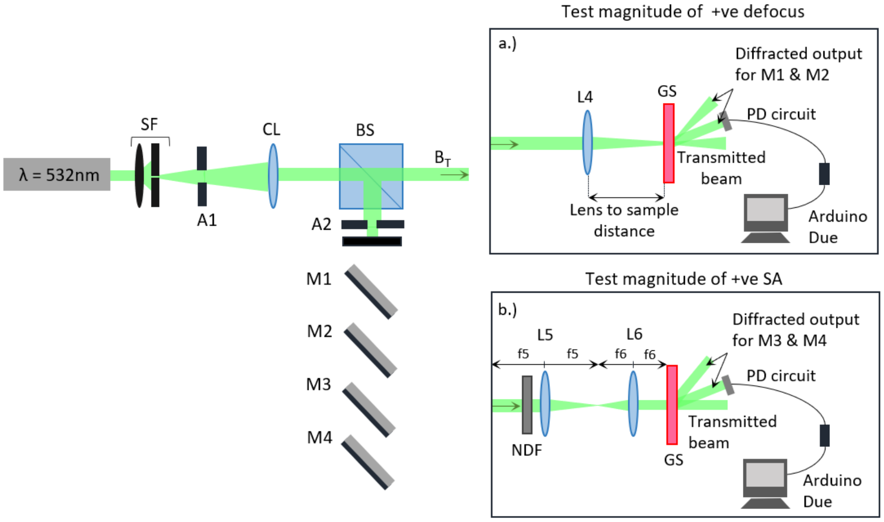

Fig. 4. Reconstruction of the HOE for measurement of (a) defocus and (b) spherical aberration, where the beam reflected off the plane mirrors was baffled and the beam normal to the sample was aberrated. A photodiode circuit, Arduino Due and a computer serial monitor were used to measure the normalized intensity ratio produced by the introduction of each test aberration.

3.3.3. Measurement of spherical aberration

A number of biconvex and plano-convex, denoted in the table below with a *, lenses, with varying focal lengths (Table 1), were arranged in a 4f system to generate four test magnitudes of spherical aberration (Fig. 4(b)).

Various entrance beam apertures were necessary to ensure that the 4 mm diameter of HOE was filled. The intensity of both the H3 and H4 spots was measured with the photodiode circuit. The normalized intensity ratio between the diffracted outputs, H3 and H4, was used to calculate the magnitude of spherical aberration. Given that the sensor was biased to detect positive spherical aberration only, a negative NIR was undefined and indistinguishable from a 0 µm SA sensing value. The magnitude of spherical aberration (W_S) contained in a wavefront was calculated by the following

$$W_S = R_S \frac{I_{H4} - I_{H3}}{I_{H4} + I_{H3}} \tag{9}$$

where $R_S = 2.85$ µm.

Table 1. Conditions required for refractive generation of spherical aberration

Beam Aperture (mm)	Focal length of L5 (mm)	Focal length of L6 (mm)	Magnitude of SA (µm)
5.7 ± 0.5	100.0	75.0	0.34 ± 0.12
6.0 ± 0.5	75.0	50.0	1.05 ± 0.36
8.0 ± 0.5	100.0	50.0	1.32 ± 0.33
5.9 ± 0.5	50.0*	35.0*	1.73 ± 0.59
7.6 ± 0.5	75.0	35.0	2.41 ± 0.61

4. Results

4.1. HOE inclusion criteria

In order to measure defocus and spherical aberration using either a single-mode or multi-mode sensor, a system was devised in which two multiplexed holograms were required for each mode. All HOEs were reconstructed with the original wavefronts used to create them, for example ±15.0 D of defocus. In this reconstruction scenario, light is diffracted into the output associated with the incoming wavefront and the NIR measured between the two diffracted outputs is ±1. However some of the light was also diffracted into the other spot required for sensing. It was found that this effect was much more prevalent in multiplexed holograms when there was a large degree of mismatch between the diffraction efficiency of the two recordings. To achieve an NIR that was as close to ±1 as possible it was necessary to equalize the diffraction efficiency of the recordings. This was particularly important for the accurate detection of other wavefront aberration magnitudes measured with the sensor. Therefore, a desired diffraction efficiency range (DER) was chosen, e.g. 35-40 %, and HOEs that varied in strength by more than $0.2 \times DER$ were excluded from the datasets.

4.2. Comparison of methods for defocus measurement

A number of wavefronts with varying magnitudes of defocus were generated to determine the sensing capability of the AHWFS. All of the aberrations were generated refractively by selecting biconvex lenses with varying optical power. The magnitudes of the aberration were as follows: +4.9 D, +7.1 D, and +9.0 D. A collimated beam was also used to generate 0 D of defocus. Classification Method 1 (CM1) of quantifying each magnitude of defocus involved mounting a lens to a cage plate on a rail and measuring the distance from the centre of the lens mount to the sample to ensure the correct aberration strength was introduced (Fig. 4(a)). The NIR at H1 and H2 was measured using the photodiode circuit. Without removing the sample from the holder, the cage plate was moved along the rail to the position associated with the next magnitude of defocus. The lens was replaced and the NIR was again measured. This was repeated for each defocus strength (Fig. 5). For Classification Method 2 (CM2), physical stops were introduced along the rail to minimize any positional inaccuracies that may have occurred when measuring the lens location for each test magnitude of defocus. This ensured that each lens was repeatedly placed at an exact distance from the HOE, and that the resultant optical power was the same for each iteration. The average percentage error was calculated for each magnitude of defocus that fell within the bounds of ±10.0 D (approximate linear region). This was carried out using the standard method of calculating percentage error as: ((experimentally determined aberration magnitude - test aberration magnitude)/test aberration magnitude) × 100. The range over which the measurement error was calculated was restricted as the response of the AHWFS was not linear towards the sensing bounds. Furthermore, the percentage error was calculated with respect to a response curve that was perfectly linear, for which 1/slope was equal to the magnitude of the bias aberration. Calibration of both the linearity and slope of the response curve will be discussed in Section 4.4. Overall, a reduction in percentage error was observed through the use of CM2. The average percentage error of all measurements was reduced from 19 % to 16 %.

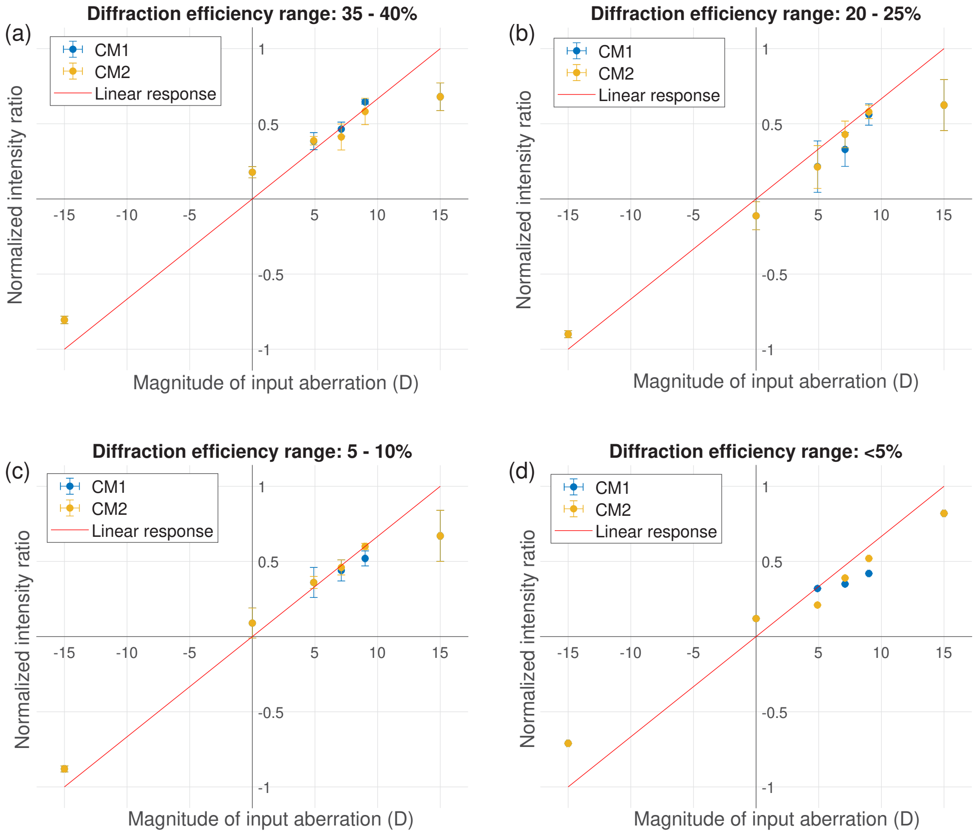

Fig. 5. Comparison of several magnitudes of defocus measured by Classification Method 1 (blue marker) and Classification Method 2 (yellow marker). The AHWFSs were fabricated with varying diffraction efficiency strengths: (a) 35-40 %, (b) 20-25 %, (c) 5-10 % and (d) <5 %.

4.3. Measurement of test magnitudes of spherical aberration

Five magnitudes of spherical aberration were generated refractively, by a combination of biconvex and plano-convex singlet lenses arranged in a 4f imaging system. The five magnitudes were 0.34 µm, 1.05 µm, 1.32 µm, 1.73 µm and 2.41 µm of positive spherical aberration over a 4 mm aperture at the image plane. The HOE was also replayed with the two bias wavefronts; 0 µm and +2.85 µm. A total of 12 HOEs were used in the measurement of each test wavefront, with each measurement repeated three times. Good convergence to a linear sensor response for aberrations in the midpoint of the sensing range (1.05 µm to 1.73 µm) was observed (Fig. 6), where the standard deviation on the NIR was small, ±0.04, ±0.03 and ±0.11 respectively. The sensing range was restricted to a region of linearity of 35 % as, again, there was an apparent loss in sensitivity to test aberrations near the sensing bounds. However, this ‘s-shaped’ response is in good agreement with behaviour theorised by Booth [32] for measurement of Zernike aberrations by a modal WFS and seen experimentally by Orlov et al. [33], Kong & Lambert [15] and Zepp & Gladysz [34] among others [14].

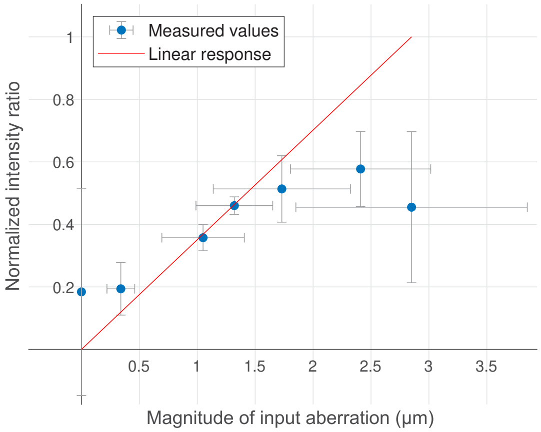

Fig. 6. Quantification of test magnitudes of refractively generated spherical aberration by a single-mode AHWFS. The vertical error bars represent the standard deviation on the average normalized intensity ratio, while the horizontal error bars show the spread in magnitude of the refractively generated SA for an aperture diameter error of ±0.5 mm. The average percentage error, ± one standard deviation, calculated for aberrations of magnitudes 1.05 µm, 1.32 µm and 1.73 µm was the absolute value of: 3.0±11.4 %, 0.7±6.0 %, and 15.4±17.5 %.

4.4. Measurement of defocus and spherical aberration by a multi-mode sensor

A multi-mode AHWFS, biased with both ±15.0 D of defocus along with 0 µm and +2.85 µm of spherical aberration, was used to detect 12 aberrated test wavefronts. Three test aberrations: +4.9 D, +7.1 D, and +9.0 D as previously, were introduced to test the defocus sensing capability of the multi-mode AHWFS. As before, the hologram was also reconstructed with wavefronts aberrated by ±15.0 D of defocus. The response of defocus channel (Fig. 7(a)) was in line with the response that had been achieved previously (Fig. 5). The measurement accuracy for the three test magnitudes of defocus was very good, with average percentage error values calculated as the absolute value of: 1.3±1.2 %, 1.3±0.1 % and 7.9±3.2 % for +4.9 D, +7.1 D and +9.0D of defocus respectively. Similar to the single-mode sensors, deviation from a linear response was observed for aberrations approaching and matching the magnitude of the sensing bounds.

As before, five test magnitudes: 0.34 µm, 1.05 µm, 1.32 µm, 1.73 µm and 2.41 µm of positive SA were used to analyse the output of the multi-mode AHWFS in response to a spherically aberrated wavefront. The nature of the response observed in the multi-mode AHWFS was similar to that of the single-mode SA sensor, however the slope of the response curve was shifted (Fig. 7(b)). As before, the percentage error was calculated with respect to a response that was perfectly linear. The average percentage error, ± one standard deviation, for aberrations of magnitudes 1.05 µm, 1.32 µm and 1.73 µm was the absolute value of: 36.6±16.2 %, 25.5±17.2 %, and 35.5±11.5 % respectively.

For both the single-mode defocus sensor and multi-mode AHWFS a reduction in sensitivity was expected for aberrations greater than approximately ±10.0 D, with the assumption that the response was similar for both +ve and -ve defocus aberrations. This corresponds to a linear response region of 66 %, within which aberrations are correctly classified with a low margin of error. For the single-mode SA sensor, approximately 35 % of the sensing range followed a linear response where aberrations were detected with an average percentage error < |15.4±17.5 %|. A difference in the linear response regions for quantification of different aberrations was expected, from theory presented by Booth [32].

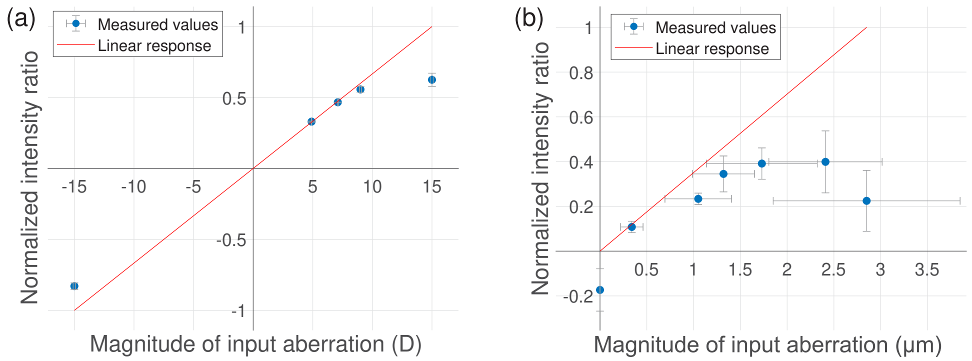

Fig. 7. Classification of (a) defocus, in dioptres and (b) spherical aberration, in μm by a multi-mode AHWFS.

In the multi-mode AHWFS, the linear response region was similar to that of the single-mode sensor at approximately 30 %. In keeping with theory, the slope of the response curve was shifted due to the presence of another aberration (defocus). In future, further calibration of the sensor response will be carried out and this apparent shift in slope will be accounted for, which will greatly reduce the measurement error of the multi-mode sensor. The number of aberration magnitudes that could be generated using refractive elements was limited, therefore an SLM will be used to further characterise and fully calibrate both the single-mode and multi-mode AHWFSs. It will be possible to tune the characteristics of this sensor to extend the region of linearity if necessary, but the similarities observed between the single-mode and multi-mode sensors for both defocus and spherical aberration detection are encouraging.

4.5. *Effect of material shrinkage during holographic recording*

A consistent shift in the Bragg reconstruction angle for HOEs recorded at 1050 and 1250 lines/mm was observed. HOEs reconstructed with a probe beam normal to the hologram fringes (B_T) had an average diffraction efficiency of approximately 5-10 %. By rotating the HOE through a small angle, with respect to B_T, an overall increase in diffraction efficiency of ~20-30 % was achieved. In general, a higher degree of rotation was required in order to maximise the diffraction efficiency of the 1250 lines/mm hologram. The central slant angle associated with the 1050 lines/mm and 1250 lines/mm hologram was 10.73° and 11.97° respectively. For the single-mode SA sensor, a rotation angle of 0.12° was required to maximise DE of the 1050 lines/mm hologram, while a 0.16° rotation angle was required at 1250 lines/mm. Therefore, a 0.14° average rotation angle was required for the measurement of test aberrations by the sensor for SA detection only. A larger rotation was required for the maximising DE of the holograms in the multi-mode AHWFS. An average rotation of 0.25° was required to achieve maximum efficiency on reconstruction. This shift in fringe spacing is likely a result of shrinkage within the material, which occurred during the holographic recording step.

Some shrinkage of this material during the holographic recording process has been observed previously [35], where it was shown that the fringe spacing is altered in the thickness direction during polymerisation. Moothanchery et al. reported a maximum shrinkage of 1.9 % in layers 60 μm thick at 1000 lines/mm, where the effect was most prevalent for lower exposure energies. A percentage shrinkage for each hologram can be determined by a ratio of the reconstruction rotation angle to fringe slant. For the single-mode SA sensor, an estimated shrinkage of 1.1 % and 1.3 % occurred at 1050 lines/mm and 1250 lines/mm respectively. The percentage shrinkage increased to 2.0 % and 2.1 % at 1050 and 1250 lines/mm respectively in the multi-mode AHWFS.

Defocus aberrations, ±15.0 D in magnitude, were previously recorded, for the fabrication of a defocus AHWFS, in 65.7±12.14 µm layers at spatial frequencies of 497 lines/mm and 816 lines/mm. A similar measurement was carried out with these samples to examine the effect of rotation angle on DE. An average increase in DE of 0.7 % was recorded. A number of factors such as carrier spatial frequency and material layer thickness may have contributed to the lower degree of shrinkage observed in the single-mode defocus sensor (see Supplemental Material).

Issues associated with any material shrinkage are negligible in holograms recorded at the lower spatial frequencies and lower layer thickness, however, for holograms with very high angular selectivity this effect may prove problematic. It is acknowledged that rotation of the HOE with respect to the incoming wavefront is not an ideal solution to this issue, particularly for measurements of complex, non-rotationally symmetric aberrations. Further study is required to measure and compare the extent of shrinkage that occurs in this and other potential materials in order to fully understand the causes for the observed shift. This will allow the optimal choice of material and, if necessary, the development of appropriate mitigation strategies.

5. Conclusion

An analog holographic wavefront sensor capable of measuring within the range of 0 µm to +2.85 µm of spherical aberration has been fabricated for the first time, in an acrylamide-based photopolymer. Five test magnitudes of positive SA were measured with the single-mode SA sensor. Aberrations with magnitudes from 1.05 µm up to 1.73 µm inclusive were measured with average percentage errors of <|15±17.5 %|. Some loss in sensitivity to magnitudes of SA approaching the sensing bounds was observed. This behaviour is in agreement with the theory and experimental results described in literature based on these holographic wavefront sensors. Additionally, the measurement accuracy of a single-mode AHWFS for defocus detection, in a range of ±15.0 D, was improved upon. The percentage error on the measurement of all wavefronts containing three magnitudes of defocus has been reduced from 19 % to 16 % with the introduction of a new method of quantifying defocus generated with conventional refractive elements. Furthermore, both a low order and high order (defocus and spherical aberration) aberration were holographically recorded in a single multiplexed analog volume phase HOE, for the fabrication of a multi-mode AHWFS, for the first time. Angular multiplexing techniques were employed to allow for the simultaneous measurement of defocus in a range of ±15.0 D and an SA range of 0 µm to +2.85 µm. A brief investigation was carried out into shrinking effects that may occur during the holographic recording process, which will guide the focus of a wider study. The linearity of both single-mode and multi-mode AHWFSs was explored and, application dependent, future work will involve tuning the sensitivity range of the multi-mode AHWFS. The successful measurement of both a low and high order aberration mode by this AHWFS is encouraging as it has been shown that both the dynamic range and sensitivity is available within the photopolymer recording material to sense multiple modes simultaneously. It is envisaged that this sensor has applications where high temporal resolution is required for studying complex ocular dynamics of the human eye; as a metrology tool on high-throughput production lines for measuring aberrations of optical components; and in adaptive optics systems for free space optical communication.

Funding. Science Foundation Ireland (18/SIRG/5666).

Acknowledgements. The authors would like to acknowledge the FOCAS Research Institute for equipment and technical support, along with colleagues in IEO for useful guidance and constructive conversations. The authors would also like extend their thanks to Dr. Alexander Goncharov for conversations regarding aberration theory.

Author contributions. KM obtained the funding for the project and supervised project direction; KM, EB, SM & MS all contributed to the experimental plan; EB carried out all experimental work; EB, KM & SM contributed to the data analysis; EB produced all Figures; EB wrote the initial manuscript draft; KM, SM & MS edited the manuscript.

Disclosures. The authors declare that there are no conflicts of interest related to this article.

Data availability. Data underlying the results presented in this paper are not publicly available at this time but may be obtained from the authors upon reasonable request.

Supplemental document. See Supplement 1 for supporting content.

References

1. M. Loktev, O. Soloviev, G. Vdovin, and S. Patlan, *OKO Guide to Adaptive Optics*, (OKO Technologies, 2013).
2. E. Brunner, J. Shatokhina, W. Drexler, R. Leitgeb, A. Pollreisz, C. K. Hitzenberger, R. Ramlau, and M. Pircher, “Retinal adaptive optics imaging with a pyramid wavefront sensor,” Biomed. Opt. Express **12**(10), 5969 (2021).
3. F. Roddier, “Curvature sensing and compensation: a new concept in adaptive optics,” Appl. Opt. **27**(7), 1223 (1988).
4. G. Dai, *Ocular Wavefront Sensing and Reconstruction*, (SPIE, 2008), Chap. 4, pp. 97–129).
5. C. Ting, C. Zhang, and Z. Yang, “Atmospheric free-space coherent optical communications with adaptive optics,” Proc. SPIE **10096**, 1009606 (2017).
6. H. Sun, N. J. Kasdin, and R. Vanderbei, “Efficient wavefront sensing for space-based adaptive optics,” J. Astron. Telesc. Instrum. Syst. **6**(1), 019001 (2020).
7. J. M. Geary, “Indirect Wavefront Measurement, Part II,” in *Introduction to Wavefront Sensors*, (SPIE, 1995), pp. 89–104.
8. B. C. Platt and R. Shack, “History and principles of Shack-Hartmann wavefront sensing,” J. Refract. Surg. **17**(5), S573–S577 (2001).
9. L.N. Thibos, “Principles of Hartmann-Shack Aberrometry,” in *Vision Science and Its Applications*, (OSA, 2000), p. NW6.
10. W. H. Southwell, “Wave-front estimation from wave-front slope measurements,” J. Opt. Soc. Am. **70**(8), 998 (1980).
11. R. Cubalchini, “Modal wave-front estimation from phase derivative measurements,” J. Opt. Soc. Am. **69**(7), 972 (1979).
12. G. Dai, “Modal wave-front reconstruction with Zernike polynomials and Karhunen–Loéve functions,” J. Opt. Soc. Am. A **13**(6), 1218 (1996).
13. M. A. A. Neil, M. J. Booth, and T. Wilson, “New modal wave-front sensor: a theoretical analysis,” J. Opt. Soc. Am. A **17**(6), 1098 (2000).
14. F. Ghebremichael, G. P. Andersen, and K. S. Gurley, “Holography-based wavefront sensing,” Appl. Opt. **47**(4), A62–A69 (2008).
15. F. Kong and A. Lambert, “Improvements to the modal holographic wavefront sensor,” Appl. Opt. **55**(13), 3615 (2016).
16. G. Andersent, “Holographic Adaptive Optics,” in *Advanced Maui Optical and Space Surveillance Technologies Conference*, E34, (2009).
17. A. Zepp, S. Gladysz, and K. Stein, “Holographic wavefront sensor for fast defocus measurement,” Adv. Opt. Technol. **2**(1), 1–2 (2013).
18. G. Andersen, L. Dussan, F. Ghebremichael, and K. Chen, “Holographic wavefront sensor,” Opt. Eng. **48**(8), 085801 (2009).
19. D. Vather, I. Naydenova, D. Cody, M. Zawadzka, S. Martin, E. Mihaylova, S. Curran, P. Duffy, J. Portillo, D. Connell, S. McDonnel, and V. Toal, “Serialized holography for brand protection and authentication,” Appl. Opt. **57**(22), E131 (2018).
20. F.-K. Bruder, T. Fäcke, and T. Rölle, “The Chemistry and Physics of Bayfol HX Film Holographic Photopolymer,” Polymers **9**(12), 472 (2017).
21. D. Cody, S. Gul, T. Mikulchyk, M. Irfan, A. Kharchenko, K. Goldyn, S. Martin, S. Mintova, J. Cassidy, and I. Naydenova, “Self-processing photopolymer materials for versatile design and fabrication of holographic sensors and interactive holograms,” Appl. Opt. **57**(22), E173 (2018).
22. T. Mikulchyk, S. Martin, and I. Naydenova, “N-isopropylacrylamide-based photopolymer for holographic recording of thermosensitive transmission and reflection gratings,” Appl. Opt. **56**(22), 6348 (2017).
23. P. Galli, R. A. Evans, C. Bertarelli, and A. Bianco, “Cyclic allylic sulfide based photopolymer for holographic recording showing high refractive index modulation,” J. Polym. Sci. **59**(13), 1399–1413 (2021).
24. E. Branigan, S. Martin, M. Sheehan, and K. Murphy, “Direct multiplexing of low order aberration modes in a photopolymer-based holographic element for analog holographic wavefront sensing,” Proc. SPIE **11860**, 16 (2021).
25. M.J. Kidger, “Aberrations,” in *Fundamental Optical Design*, (SPIE, 2001).
26. E. Branigan, S. Martin, M. Sheehan, and K. Murphy, “Modelling spherical aberration detection in an analog holographic wavefront sensor,” in *Imaging and Applied Optics Congress* p. 2 (2022).
27. M. Born and E. Wolf, “Geometrical theory of aberrations,” in *Principles of Optics*, (Cambridge University, 2003).
28. J. Wanek, M. Mori, and M. Shahidi, “The Effect of Aberrations and Scatter on Image Resolution Assessed by Adaptive Optics Retinal Section Imaging,” J. Opt. Soc. Am. A **24**(5), 1296–1304 (2007).
29. E. E. Diel, J. W. Lichtman, and D. S. Richardson, “Tutorial: avoiding and correcting sample-induced spherical aberration artifacts in 3D fluorescence microscopy,” Nat. Protoc. **15**(9), 2773–2784 (2020).
30. H. Kogelnik, “Coupled Wave Theory for Thick Hologram Gratings,” Bell Syst. Tech. J. **48**(9), 2909–2947 (1969).
31. B. Rogers, S. Martin, and I. Naydenova, “Study of the Effect of Methyldiethanolamine Initiator on the Recording Properties of Acrylamide Based Photopolymer,” Polymers **12**(4), 734 (2020).

32. M. J. Booth, "Direct measurement of Zernike aberration modes with a modal wavefront sensor," Proc. SPIE **5162**, 79–90 (2003).
33. V. V. Orlov, V. Y. Venediktov, A. V. Gorelaya, E. V. Shubenkova, and D. Z. Zhamalatdinov, "Measurement of Zernike mode amplitude by the wavefront sensor, based on the Fourier-hologram of the diffuse scattered mode," Opt. Laser Technol **116**, 214–218 (2019).
34. A. Zepp and S. Gladysz, "Fast defocus measurement for laser communications with the holographic wavefront sensor," in *Imaging and Applied Optics*, (OSA, 2013), p. OTu1A.5.
35. M. Moothanchery, I. Naydenova, and V. Toal, "Studies of shrinkage as a result of holographic recording in acrylamide-based photopolymer film," Appl. Phys. A **104**(3), 899–902 (2011).